Research Square

Preprints are preliminary reports that have not undergone peer review.
They should not be considered conclusive, used to inform clinical practice,
or referenced by the media as validated information.

Moderate Static Magnetic Field Promotes Osteoporotic Fracture Healing in OVX Mice by Enhancing Bone Remodeling and Regulating Iron Metabolism

Rui Wang
Research & Development Institute of Northwestern Polytechnical University in Shenzhen
Shenghang Wang
wangshenghang@uhrs.edu.cn

Department of Spine Surgery, People's Hospital of Longhua
Weihao Ren
Research & Development Institute of Northwestern Polytechnical University in Shenzhen
Chao Cai
Research & Development Institute of Northwestern Polytechnical University in Shenzhen
Hanyu Zhang
Research & Development Institute of Northwestern Polytechnical University in Shenzhen
Tinghua He
Research & Development Institute of Northwestern Polytechnical University in Shenzhen
Xin Zhang
Research & Development Institute of Northwestern Polytechnical University in Shenzhen
Hao Zhang
Department of Spine Surgery, People's Hospital of Longhua
Peng Shang
Research & Development Institute of Northwestern Polytechnical University in Shenzhen

Research Article

Keywords: Osteoporotic fracture, Moderate static magnetic field, Fracture healing, Post-fracture bone loss, iron metabolism

Posted Date: July 27th, 2026

DOI: https://doi.org/10.21203/rs.3.rs-10415178/v1

License: This work is licensed under a Creative Commons Attribution 4.0 International License.
Read Full License

Additional Declarations: No competing interests reported.

Abstract

Osteoporotic fractures (OPFs) exhibit impaired healing and progressive bone loss. Although moderate static magnetic fields (MMFs; 1 mT–1 T) have shown potential to regulate bone metabolism, their effects on OPF healing remain unclear. Here, we investigated the effects of MMF exposure on OPF healing and iron metabolism in OVX mice. An OVX-induced OPF model was established, and mice were exposed to 0.05–0.5 T MMF after tibial fracture. Fracture healing and bone loss were evaluated by micro-computed tomography, histological analysis, biomechanical testing, and serum biochemical assays on day 14 and 28 post-fracture. Iron contents in fracture callus, femur, and liver were determined using atomic absorption spectrometry. The results showed that MMF exposure significantly bone mineral density (BMD), improved mechanical properties, and expanded the mineralized area at the callus site in OVX mice. MMF exposure also increased osteoblast distribution and decreased osteoclast distribution at the callus site. Furthermore, MMF alleviated OVX-induced deterioration of the microarchitecture and mechanical properties of lumbar vertebrae and non-fractured tibiae, accompanied by increased serum levels of the N-terminal propeptide of type I procollagen (P1NP) and decreased levels of the β-isomer of C-terminal telopeptide of type I collagen (β-CTX). In addition, MMF regulated iron metabolism by reducing iron accumulation in fracture callus and femur and modulating serum ferritin levels during OPF healing. In conclusion, 0.05–0.5 T MMF exposure promotes OPF healing and alleviates systemic post-fracture bone loss in OVX mice and is associated with the regulation of iron metabolism, suggesting its potential as a non-invasive adjunctive therapy for OPF treatment.

Introduction

Osteoporotic fracture (OPF), a complication secondary to osteoporosis, is characterized by high incidence and significant disability and mortality rates[1]. OPF represents a major health concern for older women, with approximately 50% experiencing at least one fracture after the age of 50[2, 3]. Although current surgical and pharmacological interventions have demonstrated efficacy in treating OPF, the inherent imbalance in bone metabolism in these patients often leads to prolonged healing periods[4–7]. Moreover, studies indicate that fractures—especially in osteoporotic individuals—can induce systemic bone loss in non-fractured bones, further increasing the risk of subsequent fractures [8–10]. Therefore, developing novel strategies that simultaneously accelerate fracture repair and preserve systemic skeletal integrity is urgently needed for OPF management.

Static magnetic fields (SMFs) have shown potential clinical value by regulating bone metabolic balance[11–14].Based on magnetic flux density, SMFs can be categorized as hypomagnetic fields (HyMFs, < 5 μT), weak static magnetic fields (< 1 mT), moderate static magnetic fields (MMFs, 1 mT–1 T), and high-intensity static magnetic fields (HiSMF)[15]. MMFs have been shown to regulate bone loss and fracture healing by modulating the physiological functions of bone cells[16–18]. Our previous study demonstrated that 0.2 T–0.4 T MMF exposure promotes the restoration of bone microstructure and strength in hindlimb-unloaded (HLU) mice by inhibiting bone resorption[19]. Furthermore, 0.2–0.4 T MMF prevented the reduction of bone mineral density (BMD) and bone mineral content (BMC) and alleviated

the deterioration of bone microstructure in ovariectomized (OVX) mice[20]. In addition, 0.5 T MMF increased osteoblast distribution and reduced osteoclast distribution in the callus, thereby promoting bone formation and accelerating fracture healing in mice[21]. However, the effects of MMF exposure on OPF healing and systemic post-fracture bone loss of non-fractured bones remain unclear.

Iron homeostasis has recently emerged as an important regulator of skeletal health[22]. Iron overload and disrupted iron metabolism are recognized as common physiological alterations associated with menopause and have been implicated in the development and progression of postmenopausal osteoporosis[23, 24]. Consistently, ovariectomized (OVX) mice exhibit altered iron metabolism, suggesting a potential link between iron dysregulation and osteoporosis[25, 26]. However, whether iron metabolism contributes to delayed of OPF healing and systemic post-fracture bone loss remains unknown. Furthermore, previous studies have suggested that the regulatory effects of MMF on the bone metabolism were associated with their regulation of iron metabolism[27]. Nevertheless, whether MMF-mediated regulation of OPF healing and prevention of systemic bone loss involves modulation of iron homeostasis remains unexplored.

In this study, we investigated the effects of MMF exposure on OPF healing and post-fracture systemic bone loss using an OVX mouse model with tibial fractures. Bone microarchitecture, histological characteristics, and mechanical properties at the fracture site were evaluated during healing, while the microstructure and mechanical performance of non-fractured lumbar vertebrae and tibiae were also assessed. In addition, iron metabolism alterations were examined to explore potential mechanisms underlying MMF-mediated skeletal protection. This study provides new insights into the application of MMF as a non-invasive physical intervention for improving OPF healing and preventing post-fracture bone loss.

Materials and Methods

Construction of a MMF Exposure Device

The MMF exposure system has been previously reported in our previous study[21]. Mice were housed in cages positioned above the magnetic plate (Fig. 1A). The mouse cages were made of polypropylene (PP) material to ensure they did not interfere with the distribution of the static magnetic field. In the control group, mouse cages were similarly placed above a plate without actual magnets. Measurements using a Gauss meter showed the magnetic plate exhibited a magnetic field orientation and distribution with the N-pole facing upward (Fig. 1B). The magnetic field intensity within the fracture site of mice exposed to MMF ranged from 0.05 T to 0.5 T (located 1 cm above the magnetic plate) (Fig. 1B, C).

Modeling and Magnetic Field Exposure

This study utilized female C57BL/6 mice aged 11 weeks (Noyou Biotechnology Co., Ltd., Shaanxi, China), with body weights ranging from 22 g to 30 g. The mice were randomly divided into a control group and

OVX group. All mice were housed in an SPF facility with a temperature of 22 ± 2°C and a light/dark cycle. After one week of acclimatization, the mice bilateral ovariectomy (OVX) or sham surgery (removal the fat tissue around the bilateral ovaries) under anesthetized with isoflurane (2% in oxygen). Four weeks later, a distal tibial fracture was induced in these now 16-week-old mice under anesthesia. Following fracture modeling, the mice were further randomly divided into four subgroups, with two subgroups exposed to MMF and the remaining two serving as controls exposed to the geomagnetic field (GMF), designated as control group, MMF group, OVX group, and OVX-MMF group, respectively. On day 14 and day 28 post-fracture, the mice were euthanized for sample collection (Fig. 2A). All animal protocols used in this study were approved by the Animal Ethics and Welfare Committee of Northwestern Polytechnical University.

Serum Biochemical Analysis

Blood samples were collected and kept stationary at 4°C until serum separation. They were then centrifuged at 10,000g for 10 minutes, and the supernatant was collected to obtain serum. Serum markers of bone metabolism, including the N-terminal propeptide of type I procollagen (P1NP) and β-isomer of C-terminal telopeptide of type I collagen (β-CTX were detected using corresponding mouse ELISA kits (Jianglai Biotechnology, Shanghai, China). Meanwhile, was detected using an ELISA kit (JiangLai biological, Shanghai, China). All procedures were strictly performed according to the manufacturer's instructions.

Micro-CT

The collected fractured tibiae and lumbar vertebrae were scanned using micro-computed tomography (Micro-CT) (VivaCT80, SCANCO Medical AG, Bassersdorf, Switzerland). Scanning was performed at 70 kV, 114 μA, and 250 ms without a filter. Three-dimensional reconstruction of fracture site parameters was conducted using NRecon software (Bruker, Billerica, Massachusetts, USA). A 2 mm mid-slice (1 mm above and below the fracture line) was defined as the fracture callus region, with low-density and high-density tissues differentiated based on distinct thresholds. Microstructural parameters of the fracture region were analyzed using CTAn software (Bruker, Billerica, Massachusetts, USA). The following measurements of fracture callus structure and composition were evaluated for each specimen: BMD, bone volume fraction (BV/TV, %), trabecular thickness (Tb.Th), and trabecular number (Tb.N). The L3 lumbar vertebral trabecular bone was reconstructed and analyzed using the same software, Analysis of 0.5 mm thickness, with identical parameters and metrics as described above.

Biomechanical Testing

For the collected fractured and unfractured tibia, a three-point bending test was performed using an Instron-5943 universal testing machine (Instron 5943; Instron, Canton, MA, USA). The span between the two supports was set to 8 mm, and the loading rate was 1 mm/min until thetissuefractured. Load-displacement and stress-strain curves were generated by Instron software and MATLAB software (The

MathWorks, Inc., Natick, MA, USA) analyzed to evaluate tibial mechanical properties, including stiffness, ultimate load, ultimate displacement, bending energy absorption.

For the lumbar vertebrae, compression testing was conducted. The articular processes and spinous processes of the L4 vertebra were first removed. The cranial and caudal ends of the vertebra were polished with sandpaper until the trabecular structure of the cancellous bone was clearly exposed. The vertebral dimensions (length, width, and height) were measured using a three-dimensional ultra-depth microscope (KH-8700; HIROX, Japan). The vertebral specimen was then placed on the lower platen of the testing machine (Instron 5943; Instron, Canton, MA, USA). A compressive load was applied at a rate of 1 mm/min until deformation occurred. Load-displacement and stress-strain curves were recorded, and MATLAB software was used to calculate stiffness, ultimate load, ultimate stress, and toughness.

Histochemistry

Histochemical examinations of the fracture callus were performed at 14 and 28 days post-fracture. The fractured tibia were fixed in 4% paraformaldehyde for 48 hours and decalcified with 10% EDTA. Subsequently, the specimens were embedded in paraffin and sectioned into 5 μm-thick slices. Safranin O/Fast Green (SFO/FG) staining was used to detect the distribution of cartilage and mineralized regions within the callus, with cartilage tissue stained red and mineralized bone tissue stained green.

Hematoxylin and eosin (H&E) staining was performed to assess the basic morphology of the fracture callus and quantify osteoblasts, which appeared as elongated spindle-shaped cells adherent to trabecular bone surfaces. Tartrate-resistant acid phosphatase (TRAP) staining (Sigma-Aldrich, Burlington, MA, USA) was employed to evaluate osteoclasts in the fracture callus, with osteoclasts stained red. The number of osteoblasts per bone surface (N.Ob/BS), number of osteoclasts per bone surface (N.Oc/BS), and osteoclast surface per bone surface (Oc.S/BS) were analyzed by personnel with over 5 years of experience in histomorphometric evaluation following established protocols.

Determination of iron in tissues

The iron in the callus, liver, and femora were determined using an atomic absorption spectrometry (AAS; Analytik Jena, Jena, Germany). The tissues were collected from the sacrificed mice after the cardiac perfusion by normal saline solution. Dried the tissues under 120 ℃ for 6 hours, and measured its dry weight. After that, heated the tissues at 600 ℃ for 6 hours to ash the tissue, then dissolved in 1 ml 65% HNO_3. Dilute the samples with ddH_2O to a suitable concentration, then the iron concentration were measured by flame AAS. The iron content in tissues was calculated as the mass fraction between the mass of the element and tissue dry weight, respectively.

Statistical Analysis

All statistical analyses were performed using GraphPad Prism statistical software (Version 10, GraphPad Software Inc., San Diego, CA, USA). Data are presented as mean ± standard deviation. The Shapiro-Wilk normality test was used to assess normal distribution, with $P > 0.05$. Differences among multiple treatment groups were analyzed using one-way ANOVA. For all statistical tests, $P < 0.05$ was considered to indicate statistical significance.

Results

Effects of MMF Exposure on Bone Microstructure of Fracture Callus in OVX Mice

Fracture healing at the surgical site was evaluated via micro-CT analysis on day 14 and day 28 post-fracture. Micro-CT reconstruction images revealed that on day 14, both the control and OVX groups exhibited distinct fracture gaps. However, compared to the OVX group, the OVX-MMF group showed a relatively narrower gap and larger callus volume (Fig. 2B, C). On day 28, the fracture line in the Sham group was nearly bridged, whereas the OVX group still displayed visible fracture lines. In contrast, MMF treatment significantly improved fracture reconnection (Fig. 2B,C). Statistical analysis revealed that OVX treatment significantly reduced the BMD and Tb.N of fracture callus on day 14 and day 28 post-fracture (Fig. 2D). MMF exposure improved BMD and BV/TV of fracture callus on day 14, and enhanced BMD, BV/TV, Tb.N, and Tb.Th on day 28 in OPF mice (Fig. 2D). In addition, MMF exposure also increased BV/TV, Tb.N, and Tb.Th of fracture callus during the fracture healing process in sham-OVX mice (Fig. 2D).

Effects of MMF Exposure on Cartilage/Mineralized Bone Matrix and Mechanical Properties of Fracture Callus

Safranin O stains cartilage tissue red, while mineralized bone is dyed green by fast green (Fig. 3A). Histomorphometric analysis revealed OVX treatment reduced the Cg.Ar./Ps.Cl.Ar.% at the fracture site on day 14 but increased it on day 28 (Fig. 3B). Additionally, OVX decreased the Md.Ar./Ps.Cl.Ar.% throughout the healing process. MMF exposure increased the Cg.Ar./Ps.Cl.Ar.% on day 14 and the Md.Ar./Ps.Cl.Ar.% on both day 14 and day 28 of fracture callus in OVX mice (Fig. 3B, C). Furthermore, MMF exposure reduced the Cg.Ar./Ps.Cl.Ar.% on day 28 in OVX mice (Fig. 3B).

The mechanical performance of fractured tibiae after 4-week fracture healing under MMF exposure was evaluated using the three-point bending test (Fig. 3D). The results showed that OVX treatment significantly reduced the stiffness, ultimate load, and bending energy absorption at the fracture site in mice. MMF exposure increased the stiffness, ultimate load, and bending energy absorption of fracture callus in OVX mice. Additionally, MMF exposure also enhanced the ultimate load and ultimate displacement at the fracture site in sham-OVX mice.

Effects of MMF Exposure on bone turnover in OVX fractured Mice

Osteoblasts on callus trabecular bone surfaces are illustrated (Fig. 4A). Statistical analysis showed that the OVX-MMF group exhibited a significantly higher N.Ob/BS compared to the OVX group on day 28 post-fracture (Fig. 4B). TRAP staining visualized osteoclast distribution on callus trabecular surfaces (Fig. 4C). Statistical analysis demonstrated that compared with the control group, the OVX treatment increased in N.Oc/BS and Oc.S/BS at the fracture site on day 14, as well as an increased N.Oc/BS on day 28 post-fracture (Fig. 4D, E). MMF exposure significantly reduced Oc.S/BS at the fracture site on day 28 in OVX mice. Notably, MMF exposure significantly increased Oc.S/BS at the fracture site on day 14 in OVX group mice compared to the control group (Fig. 4E).

Serum bone formation marker P1NP and bone resorption marker β-CTX were measured on day 14 and day 28 post-fracture. Results showed that MMF exposure increased serum P1NP levels on day 28 post-fracture in sham-OVX mice, but had no significant effect in OPF mice (Fig. 4F). MMF exposure significantly reduced β-CTX levels in OVX mice on day 14 post-fracture (Fig. 4G).

Effects of MMF Exposure on Microstructure and Mechanical Properties of Non-fractured Bones in OVX Mice with Tibial Fractures

Micro-CT analysis of the lumbar vertebrae was used to evaluate the effects of MMF exposure on the microarchitecture of non-fractured bones during OPF healing in OVX mice. The reconstructed micro-CT images of the lumbar L3 vertebrae were shown in Fig. 5A. Analysis of trabecular microstructural parameters demonstrated that compared to the control group, OVX mice exhibited lower BMD, BV/TV, Tb.N, and Tb.Th of lumbar vertebrae during the fracture healing process (Fig. 5B). Notably, MMF exposure significantly increased BMD, BV/TV, Tb.N, and Tb.Th of lumbar vertebrae on day 28 post-fracture in OVX mice (Fig. 5B).

Subsequently, lumbar vertebrae and non-fractured tibia were subjected to compression and three-point bending tests, respectively, to evaluate the effects of MMF exposure on the mechanical properties of non-fractured bones during OPF healing. The results showed that OVX treatment significantly reduced the mechanical properties of lumbar vertebrae and non-fractured tibia in mice, including stiffness, ultimate load, and bending energy absorption. MMF exposure enhanced stiffness, ultimate load, ultimate stress, and toughness in OVX mice during OPF healing (Fig. 5C). Furthermore, MMF exposure significantly increased the ultimate load of non-fractured tibiae in OVX mice on day 14 and day 28 post-fracture (Fig. 5D). Moreover, MMF exposure enhanced stiffness, ultimate stress, and toughness of the non-fractured tibiae on day 28 post-fracture in OVX mice (Fig. 5D).

Effects of MMF Exposure on iron metabolism in OVX Mice with Tibial Fractures

Accumulating evidence suggests that the regulation of bone metabolism by static magnetic fields is closely associated with alterations in iron homeostasis. In the present study, atomic absorption spectrometry was employed to determine the iron content in the fracture callus, femur, and liver of mice subjected to MMF exposure following tibial fracture. The results showed that OVX significantly increased iron accumulation in the fracture callus on day 14 post-fracture (Fig. 6A). MMF exposure significantly reduced callus iron levels in OVX mice on day 28 during fracture healing (Fig. 6B). Furthermore, OVX markedly increased iron content in the femur of fractured mice, whereas MMF exposure significantly decreased femoral iron levels in OPF mice (Fig. 6C, D). Analysis of liver iron levels revealed that neither OVX nor MMF exposure significantly affected liver iron content on day 14 after fracture (Fig. 6E, F). Nevertheless, OVX significantly decreased liver iron content on day 28 post-fracture. In addition, serum ferritin levels were assessed to further evaluate systemic iron metabolism. As shown in Fig. 6, OVX significantly increased serum ferritin levels on day 14 after fracture but markedly decreased serum ferritin levels on day 28 post-fracture (Fig. 6G, H). Notably, MMF exposure significantly reduced serum ferritin levels in OPF mice on day 14 post-fracture.

Discussion

OPF remains a major clinical challenge because impaired bone remodeling not only delays fracture repair but also predisposes patients to progressive bone loss and secondary fractures[28, 29]. This study demonstrates that whole-body 0.05–0.5 T MMF exposure simultaneously accelerates OPF healing and mitigates fracture-induced systemic bone loss in OVX mice. Specifically, MMF enhanced callus mineralization and mechanical strength, promoted bone remodeling at the fracture site, preserved the microarchitecture and mechanical properties of non-fractured bones, and modulated iron metabolism during fracture healing. Collectively, these findings suggest that MMF exerts both local and systemic skeletal protective effects during osteoporotic fracture repair.

Numerous animal studies have shown that fracture healing takes longer under osteoporotic conditions, and clinical studies have similarly reported a negative correlation between osteoporosis and fracture healing outcomes [7, 30, 31]. Consistent with previous animal studies and clinical observations, in this study, the OVX mice exhibited reduced BMD, deteriorated bone microarchitecture, inferior mechanical properties, and delayed callus maturation compared with sham-OVX controls. Histological analysis further demonstrated reduced Md.Ar./Ps.Cl.Ar.% and prolonged cartilage retention within the fracture callus, indicating delayed endochondral ossification in OPF mice. Furthermore, MMF exposure increased the Md.Ar./Ps.Cl.Ar.% and decreased Cg.Ar./Ps.Cl.Ar.% at the fracture callus in OPF mice. These results suggest that MMF exposure alleviate OVX-induced delayed fracture healing by promoting the transition from cartilaginous to mineralized callus.

Fracture healing requires coordinated regulation of osteoblast-mediated bone formation and osteoclast-mediated bone resorption[32]. Numerous studies have shown that MMFs have a protective effect on hind limb unloading (HLU) and OVX induced bone loss in mice[16, 19]. Meanwhile, our previous study showed that MMF exposure promoted osteogenesis and suppressed osteoclastogenesis during fracture

healing in male mice[21]. In this study, 0.05–0.5 T MMF exposure significantly increased the distribution of osteoblasts at the fracture callus on day 28 post-OPF. Interestingly, MMF exposure increased serum P1NP level in fractured sham-OVX mice, while MMF exposure did not significantly alter serum P1NP levels in OPF mice. This discrepancy may reflect the difference between local and systemic bone formation in OPF mice, as histomorphometric analysis primarily reflects osteogenic activity at the fracture site, whereas circulating P1NP represents whole-body bone formation. Therefore, local osteogenesis during fracture healing may be more sensitive to MMF exposure than systemic bone formation in OVX mice. In addition, MMF exposure did not significantly reduce osteoclast distribution at the fracture callus but significantly decreased serum bone resorption marker β-CTX levels on day 14 post-fracture in mice. This finding suggests that MMF may preferentially suppress systemic osteoclast activity rather than reducing osteoclast abundance within the fracture callus in the early stage of fracture healing. Because osteoclast-mediated remodeling is essential for removal of mineralized cartilage during fracture healing. Therefore, the ability of MMF to reduce systemic bone resorption while largely preserving local osteoclast distribution may represent a favorable balance that supports efficient fracture healing without disrupting physiological callus remodeling.

Secondary fractures are a serious consequence of osteoporosis, with reported refracture rates of 9% within 1 year and 20% within 5 years after the initial fracture [33, 34]. Fracture-induced acute post-traumatic bone loss is one of the major contributors to secondary fractures[8]. In this study, the progressive deterioration of lumbar trabecular microarchitecture and mechanical properties were observed in OPF mice. MMF exposure significantly improved lumbar trabecular microarchitecture and enhanced the mechanical properties of both lumbar vertebrae and non-fractured tibiae, accompanied by reduced serum β-CTX levels in OPF mice. These results suggest that whole-body MMF exposure not only accelerates local fracture healing but also exerts beneficial systemic effects by mitigating fracture-induced bone loss in non-fractured bones.

Iron metabolism plays an important role in bone metabolism[22, 35]. Excessive iron accumulation has been shown to impair osteoblast differentiation, promote osteoclastogenesis, increase oxidative stress, and ultimately accelerate bone loss[36, 37]. Both postmenopausal women and OVX mice exhibit disrupted iron metabolism, which has been recognized as an important contributor to osteoporosis progression [38]. Previous studies indicated that MMF regulates iron homeostasis during osteoporosis development and fracture healing[21, 27, 39]. In this study, 0.05–0.5 T MMF exposure reduced iron content in the fracture callus and femur and modulated serum ferritin levels during fracture healing in OPF mice. This suggests that the promoting effect of MMF on OPF healing and its protective effect on post-fracture systemic bone loss may be related to its regulation of iron metabolism in bone tissue. However, whether iron metabolism is a direct mediator of MMF-enhanced OPF healing requires further investigation using pharmacological or genetic approaches targeting iron metabolism.

This study still has some limitations. Firstly, in this study we only investigated the effect of MMF on the healing status of postmenopausal osteoporotic fractures simulated by OVX mice, but further research is needed on its impact on OPF healing under aging and disuse bone loss conditions. Secondly, although

alterations in iron metabolism were observed, the molecular mechanisms linking MMF exposure, iron metabolism, and OPF healing still need to further investigate.

In conclusion, whole-body 0.05–0.5 T MMF exposure promotes OPF healing while mitigating fracture-induced systemic bone loss in OVX mice. These beneficial effects are associated with enhanced bone remodeling and modulation of iron metabolism. These findings contribute to a more comprehensive understanding of effects of MMFs on bone and provide a theoretical foundation for their potential clinical application in enhancing fracture healing in postmenopausal osteoporotic patients.

Declarations

Acknowledgements

This work was supported by the Shenzhen Science and Technology Program under Grant [JCYJ20230807144159004] and Guangdong Basic and Applied Basic Research under Grant [2022A1515110171].

Disclosure statement

The authors report there are no competing interests to declare.

Author Contribution

Conceptualization, R.W, SH.W. and P.S.; methodology, R.W and SH.W; software, SH.W. and HY.Z.; validation, SH.W. and TH.H.; formal analysis, C.C, TH.H, and HY.Z.; investigation, SH.W, HY.Z, R.W, WH.R, C.C, and X.Z; resources, SH.W, and P.S.; data curation, SH.W, R.W, WH.R, and TH.H; writing—original draft preparation, R.W and SH.W; writing—review and editing, SH.W, H.Z and P.S.; visualization, SH.W; supervision, SH.W, H.Z and P.S.; project administration, SH.W.; funding acquisition, SH.W

References

1. Kendler DL et al (2018) Effects of teriparatide and risedronate on new fractures in post-menopausal women with severe osteoporosis (VERO): a multicentre, double-blind, double-dummy, randomised controlled trial. Lancet 391(10117):230–240
2. Hernlund E et al (2013) Osteoporosis in the European Union: medical management, epidemiology and economic burden. A report prepared in collaboration with the International Osteoporosis Foundation (IOF) and the European Federation of Pharmaceutical Industry Associations (EFPIA). Arch Osteoporos 8(1):136
3. Zhou J, Hua X, Tang J (2020) *Diagnosis,treatment and prevention of osteoporotic fracture.* J Clin Intern Med, 37(5): p. 4. Chinese

4. Sundeep K (2019) Current state of science on drug therapies for osteoporotic fracture prevention. Innov Aging, 3(S1)
5. Olson JJ, Dyer GSM (2021) Skinny wire and locking plate fixation for comminuted intra-articular distal humerus fractures: a technical trick and case series. JSES Rev Rep Tech 1(1):34–40
6. Sing CW et al (2023) Global Epidemiology of Hip Fractures: Secular Trends in Incidence Rate, Post-Fracture Treatment, and All-Cause Mortality. J Bone Min Res 38(8):1064–1075
7. Chandran M et al (2024) Impact of osteoporosis and osteoporosis medications on fracture healing: a narrative review. Osteoporos Int 35(8):1337–1358
8. Zheng XQ et al (2023) Pathophysiological mechanism of acute bone loss after fracture. J Adv Res 49:63–80
9. Fischer V et al (2018) Calcium and vitamin D in bone fracture healing and post-traumatic bone turnover. Eur Cell Mater 35:365–385
10. Osipov B et al (2024) Altered post-fracture systemic bone loss in a mouse model of osteocyte dysfunction. JBMR Plus 8(12):ziae135
11. Wang J et al (2024) A 0.2 T-0.4 T Static Magnetic Field Improves the Bone Quality of Mice Subjected to Hindlimb Unloading and Reloading Through the Dual Regulation of BMSCs via Iron Metabolism. Int J Mol Sci, 25(23)
12. Zhang J et al (2018) Effects of static magnetic fields on bone microstructure and mechanical properties in mice. Electromagn Biol Med 37(2):76–83
13. Filippi M et al (2019) Magnetic nanocomposite hydrogels and static magnetic field stimulate the osteoblastic and vasculogenic profile of adipose-derived cells. Biomaterials 223:119468
14. Wu D et al (2023) Correction: Bone mesenchymal stem cells stimulation by magnetic nanoparticles and a static magnetic field: release of exosomal miR-1260a improves osteogenesis and angiogenesis. J Nanobiotechnol 21(1):217
15. Wang S et al (2019) Safety of exposure to high static magnetic fields (2 T-12 T): a study on mice. Eur Radiol 29(11):6029–6037
16. Zhang H et al (2018) Moderate-intensity 4mT static magnetic fields prevent bone architectural deterioration and strength reduction by stimulating bone formation in streptozotocin-treated diabetic rats. Bone 107:36–44
17. Kim EC et al (2015) Effects of moderate intensity static magnetic fields on human bone marrow-derived mesenchymal stem cells. Bioelectromagnetics 36(4):267–276
18. Kim EC et al (2018) Effects of moderate intensity static magnetic fields on osteoclastic differentiation in mouse bone marrow cells. Bioelectromagnetics 39(5):394–404
19. Yang J et al (2021) Static magnetic field of 0.2–0.4 T promotes the recovery of hindlimb unloading-induced bone loss in mice. Int J Radiat Biol 97(5):746–754
20. Yang J et al Moderate Static Magnetic Fields Prevent Bone Architectural Deterioration and Strength Reduction in Ovariectomized Mice. IEEE Trans Magn, 2021(57 – 7 Pt.2).

21. Wang S et al (2023) Moderate static magnetic field promotes fracture healing and regulates iron metabolism in mice. Biomed Eng Online 22(1):107
22. Zhang H et al (2024) The influence of iron on bone metabolism disorders. Osteoporos Int 35(2):243–253
23. Merlo F et al (2023) Changes in Iron Status Biomarkers with Advancing Age According to Sex and Menopause: A Population-Based Study. J Clin Med, 12(16)
24. Li GF et al (2023) Role of Iron Accumulation in Osteoporosis and the Underlying Mechanisms. Curr Med Sci 43(4):647–654
25. Hou Y et al (2012) Estrogen regulates iron homeostasis through governing hepatic hepcidin expression via an estrogen response element. Gene 511(2):398–403
26. Gong P et al (2026) Macrophage iron overload promotes osteoporosis via Cxcl3- and Cxcl7-mediated paracrine signaling in ovariectomized mice. J Orthop Translat 56:101008
27. Zhen C et al (2025) Moderate static magnetic field regulates iron metabolism and salvage bone loss caused by iron accumulation. J Orthop Translat 50:144–157
28. Saul D, Khosla S (2022) Fracture Healing in the Setting of Endocrine Diseases, Aging, and Cellular Senescence. Endocr Rev 43(6):984–1002
29. Steppe L et al (2023) Fracture healing research: Recent insights. Bone Rep 19:101686
30. Singh M, Nagrath AR, Maini PS (1970) Changes in trabecular pattern of the upper end of the femur as an index of osteoporosis. J Bone Joint Surg Am 52(3):457–467
31. Gorter EA et al (2020) Does osteoporosis affect the healing of subcapital humerus and distal radius fractures? J Orthop 22:237–241
32. Cao B et al (2025) Salvianolic acid A promotes bone-fracture healing via balancing osteoblast and osteoclast differentiation. FASEB J 39(2):e70364
33. Sujic R et al (2019) Five-year refracture rates of a province-wide fracture liaison service. Osteoporos Int 30(8):1671–1677
34. Yanping J et al Quality of Life and Its Influencing Factors in Elderly Patients with Osteoporotic Hip Fractures After Surgery. Chin Nurs Manage, 2016(9): p. 6
35. Yang Y et al (2026) The Interaction Between Iron Overload and Lead Exposure on Bone Metabolism. Front Biosci (Landmark Ed) 31(6):50432
36. Tang X et al (2025) Inhibition of ferroptosis rescues BMP osteogenic differentiation impaired by iron overload in the osteoporotic microenvironment. Cell Signal 136:112116
37. Passin V et al (2025) Depletion of macrophages and osteoclast precursors mitigates iron overload-mediated bone loss. IUBMB Life 77(1):e2928
38. Jiang Z et al (2024) Ferroptosis in Osteocytes as a Target for Protection Against Postmenopausal Osteoporosis. Adv Sci (Weinh) 11(12):e2307388
39. Xue Y et al (2020) Disorder of Iron Metabolism Inhibits the Recovery of Unloading-Induced Bone Loss in Hypomagnetic Field. J Bone Min Res 35(6):1163–1173

Figures

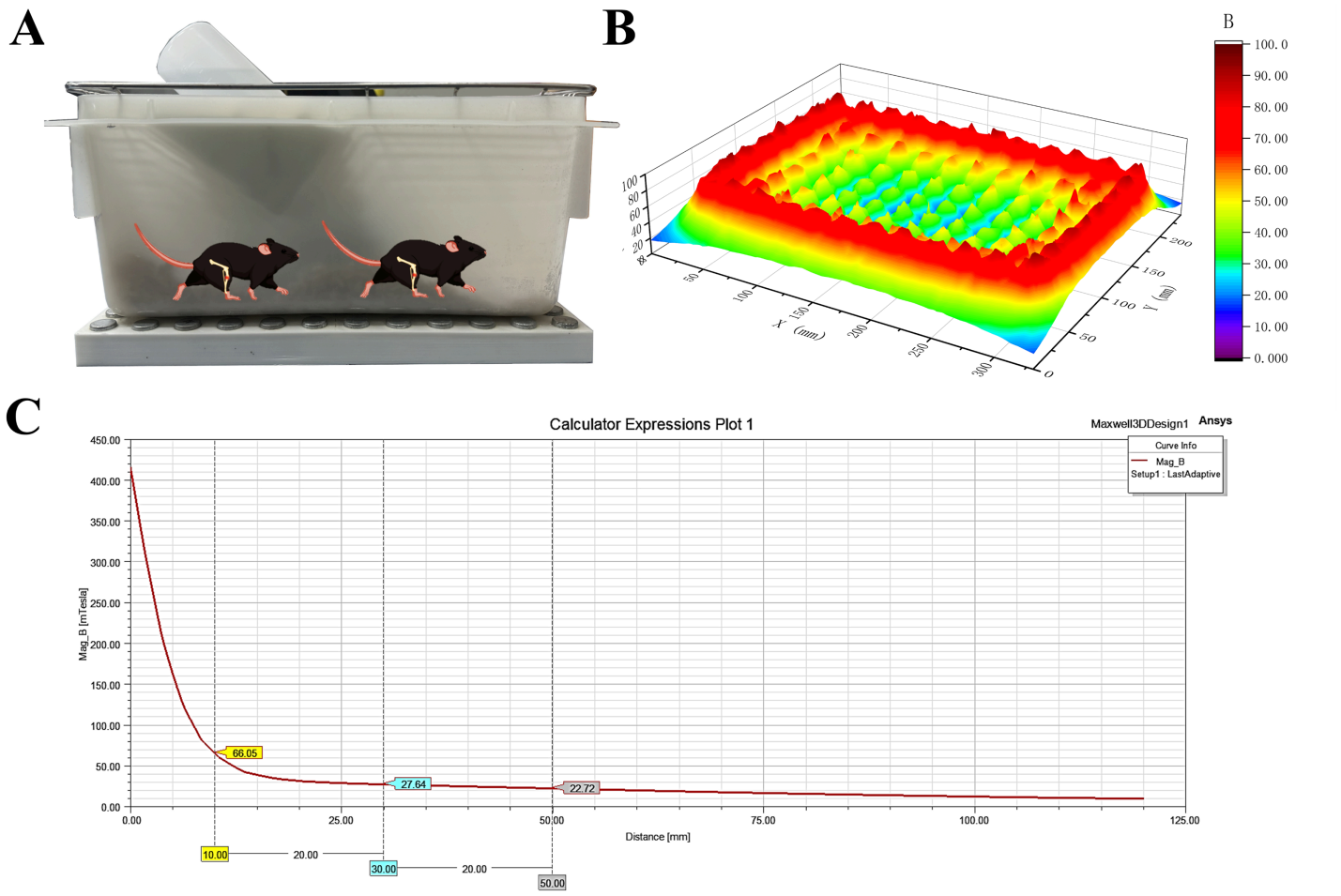


Figure 1

The MMF Exposure System for Mice. (**A)** Relative position of mice during MMF exposure. (**B)**Magnetic field intensity distribution at 1 cm above the magnetic plate. (**C)**Gradient variation of magnetic field intensity with height.

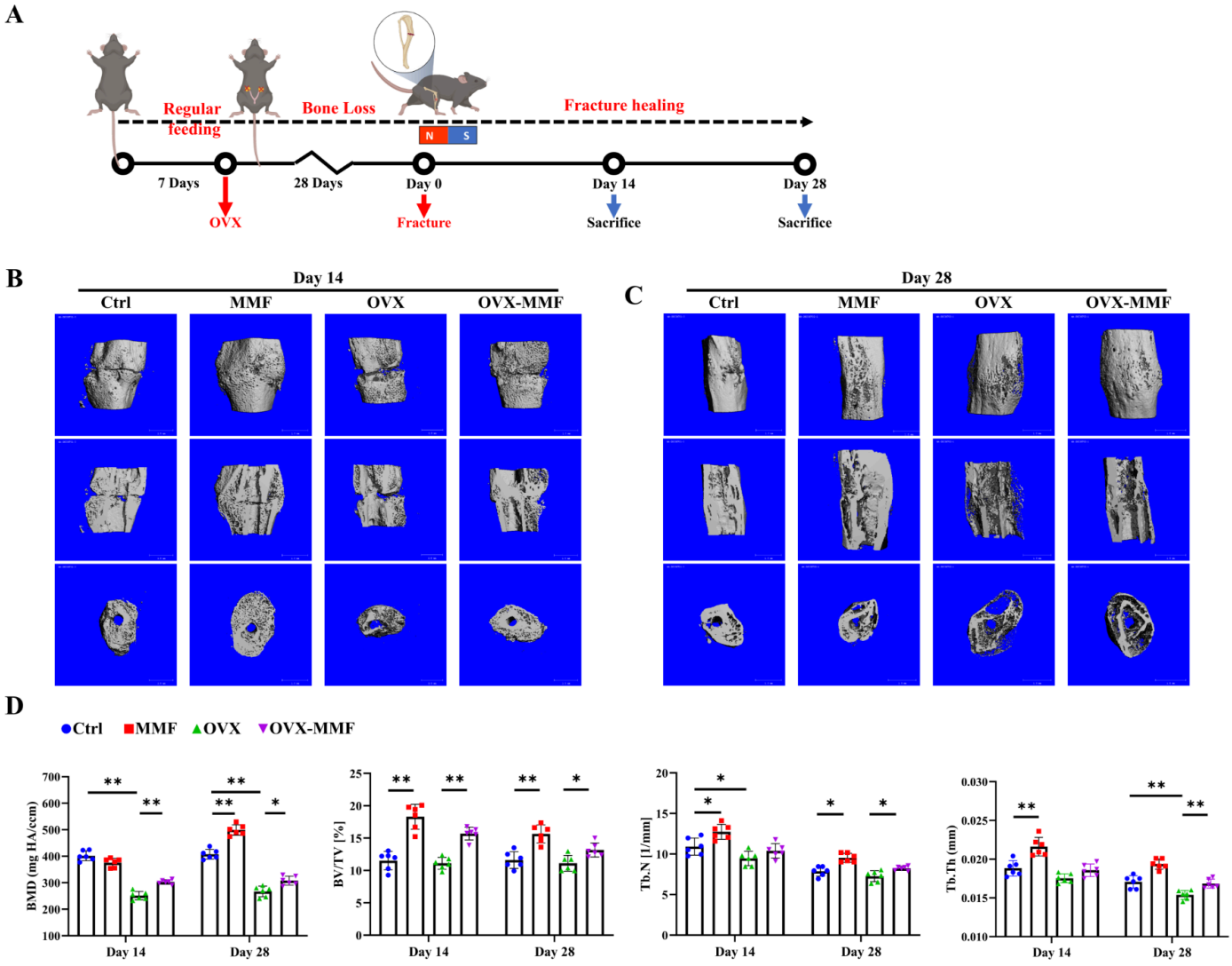


Figure 2

Effects of MMF Exposure on Bone Microstructure of Fracture Callus in OVX Mice. (**A**)Mouse Experimental Procedures for Husbandry, OVX Modeling, Fracture Modeling, MMF Magnetic Field Exposure, and Sample Collection and Testing. (**B, C**) Representative 3D micro-CT scans of tibial fractures, including the overall appearance and sagittal plane at 1 mm above and below the fracture line, as well as the transverse section at the fracture site. (**D**) Quantitative analysis of structural parameters of the fracture callus: bone mineral density (BMD), bone volume fraction (BV/TV), trabecular thickness (Tb.Th), and trabecular number (Tb.N). n=6. Data represents the mean ± SD. *P<0.05, **P<0.01.

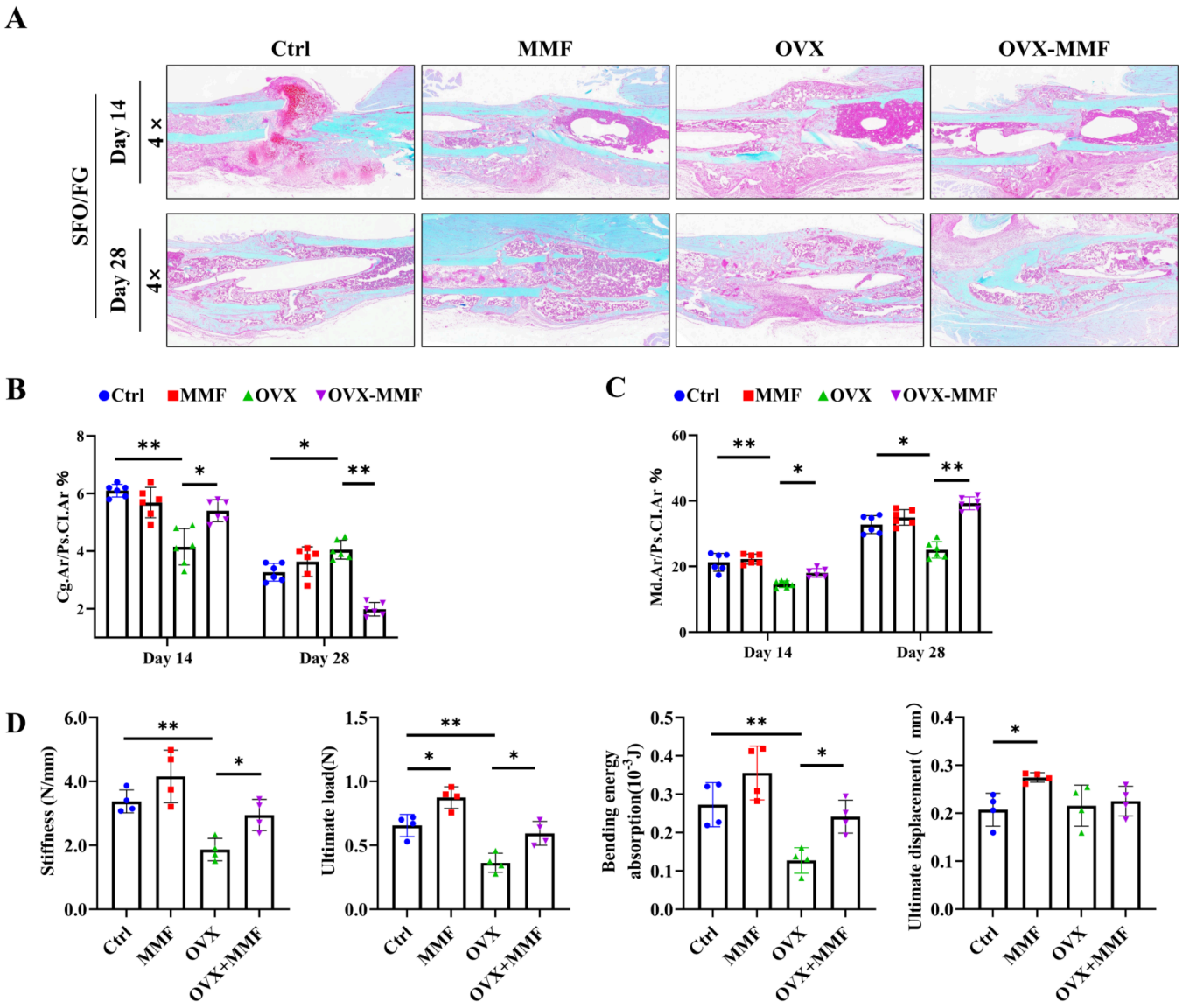


Figure 3

Effects of MMF Exposure on Cartilage/Mineralized Bone Matrix and Mechanical Properties of Fracture Callus in OVX Mice. (A) Representative images of Safranin O/Fast Green (SFO/FG)-stained paraffin sections showing the cartilaginous region (red-positive area stained by SFO) and mineralized region (green-positive area stained by FG) in the fracture callus. **(B, C)** Histomorphometric quantification of the cartilage area-to-periosteal callus area ratio (Cg.Ar./Ps.Cl.Ar.%) **(B)**and mineralized area-to-periosteal callus area ratio (Md.Ar./Ps.Cl.Ar.%) **(C)**between the control and MMF-exposed groups during fracture healing. **(D)** Structural mechanical properties of fractured tibiae were determined via three-point bending tests, including stiffness, ultimate load, ultimate displacement, and bending energy absorption. Scale bars: 100 μm. n≥4. Data represents the mean ± SD. **P*<0.05, ***P*<0.01.

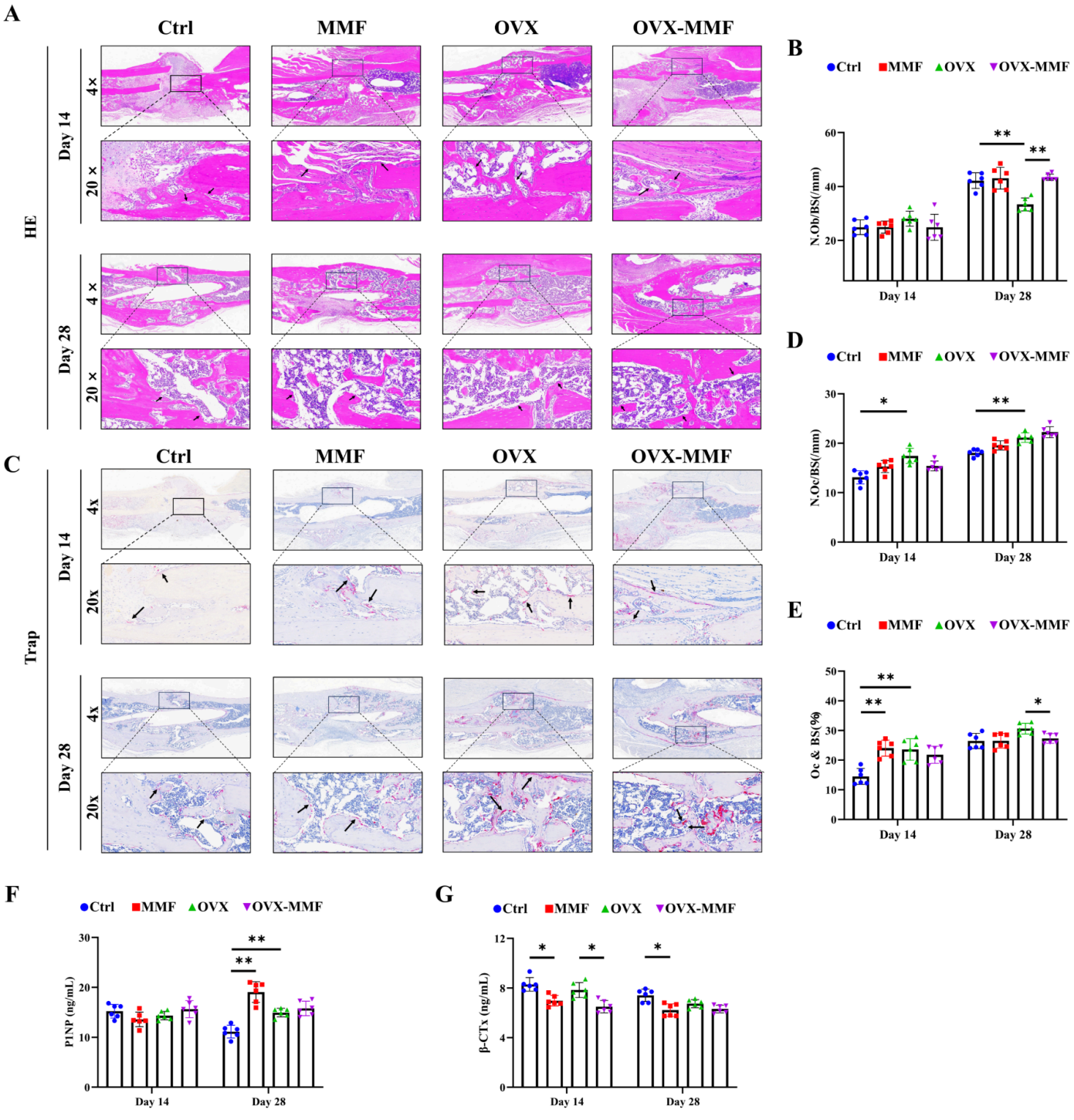


Figure 4

Effects of MMF Exposure on Cartilage/Mineralized Bone Matrix and Mechanical Properties of Fracture Callus in OVX Mice. (A) Representative images of Safranin O/Fast Green (SFO/FG)-stained paraffin sections showing the cartilaginous region (red-positive area stained by SFO) and mineralized region (green-positive area stained by FG) in the fracture callus. **(B, C)** Histomorphometric quantification of the cartilage area-to-periosteal callus area ratio (Cg.Ar./Ps.Cl.Ar.%) **(B)**and mineralized area-to-periosteal callus area ratio (Md.Ar./Ps.Cl.Ar.%) **(C)**between the control and MMF-exposed groups during fracture

healing. **(D)** Structural mechanical properties of fractured tibiae were determined via three-point bending tests, including stiffness, ultimate load, ultimate displacement, and bending energy absorption. Scale bars: 100 μm. n≥4. Data represents the mean ± SD. *P<0.05, **P<0.01.

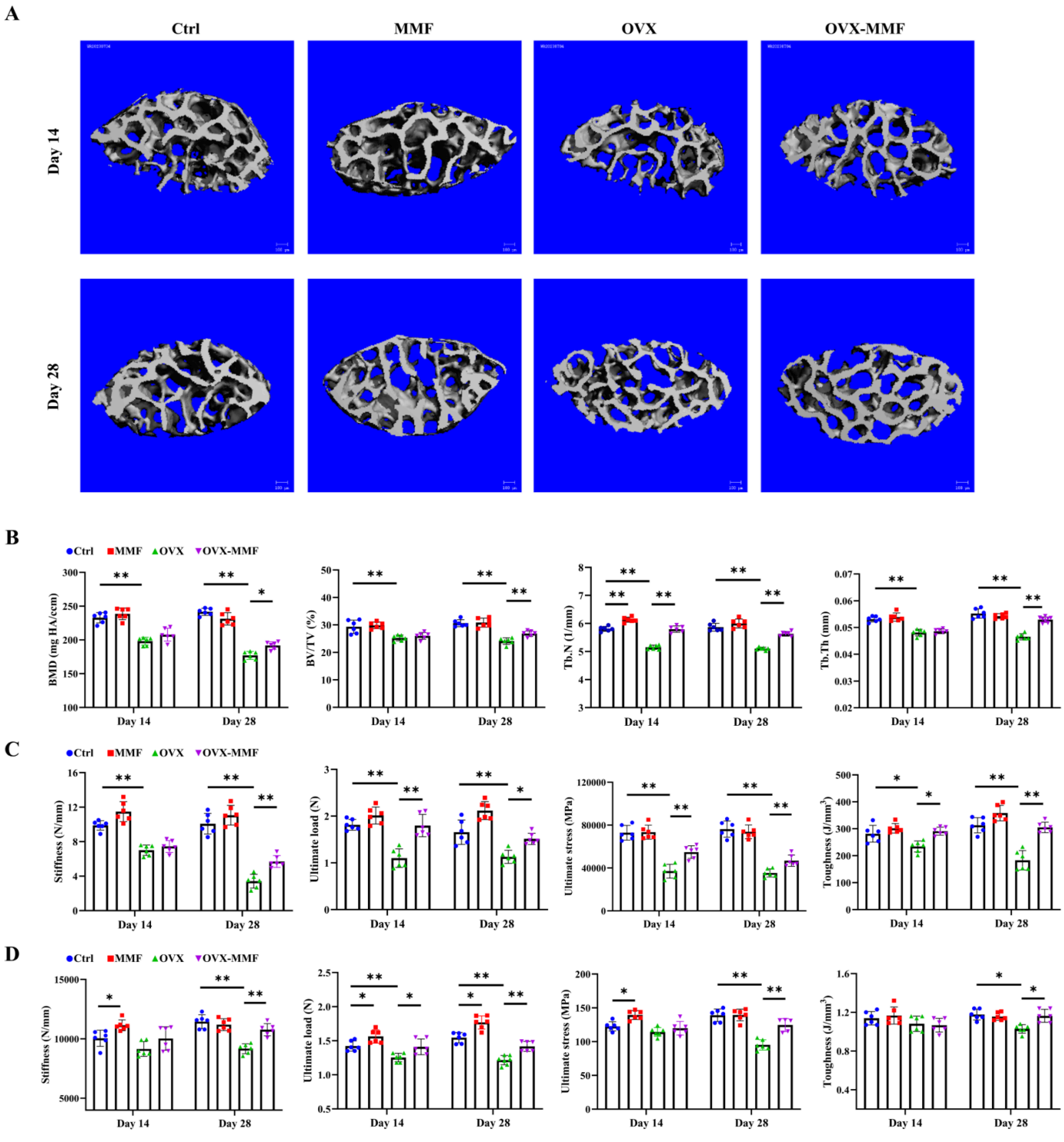


Figure 5

Effects of MMF Exposure on Microstructure and Mechanical Properties of Non-fractured Bones in OVX Mice with Tibial Fractures. (A) Representative 3D reconstructed micro-CT images of trabecular bone cross-sections in lumbar vertebra L3. **(B)** Quantitative analysis of trabecular structural parameters in L3, including bone mineral density (BMD), bone volume fraction (BV/TV), trabecular number (Tb.N), and trabecular thickness (Tb.Th). **(C)**Mechanical compression testing of L4 vertebrae with derived parameters stiffness, ultimate load, ultimate stress, and toughness. **(D)**Three-point bending testing of non-fractured tibiae with derived parameters stiffness, ultimate load, ultimate stress, and toughness. n=6. Data represents the mean ± SD. *P<0.05, **P<0.01.

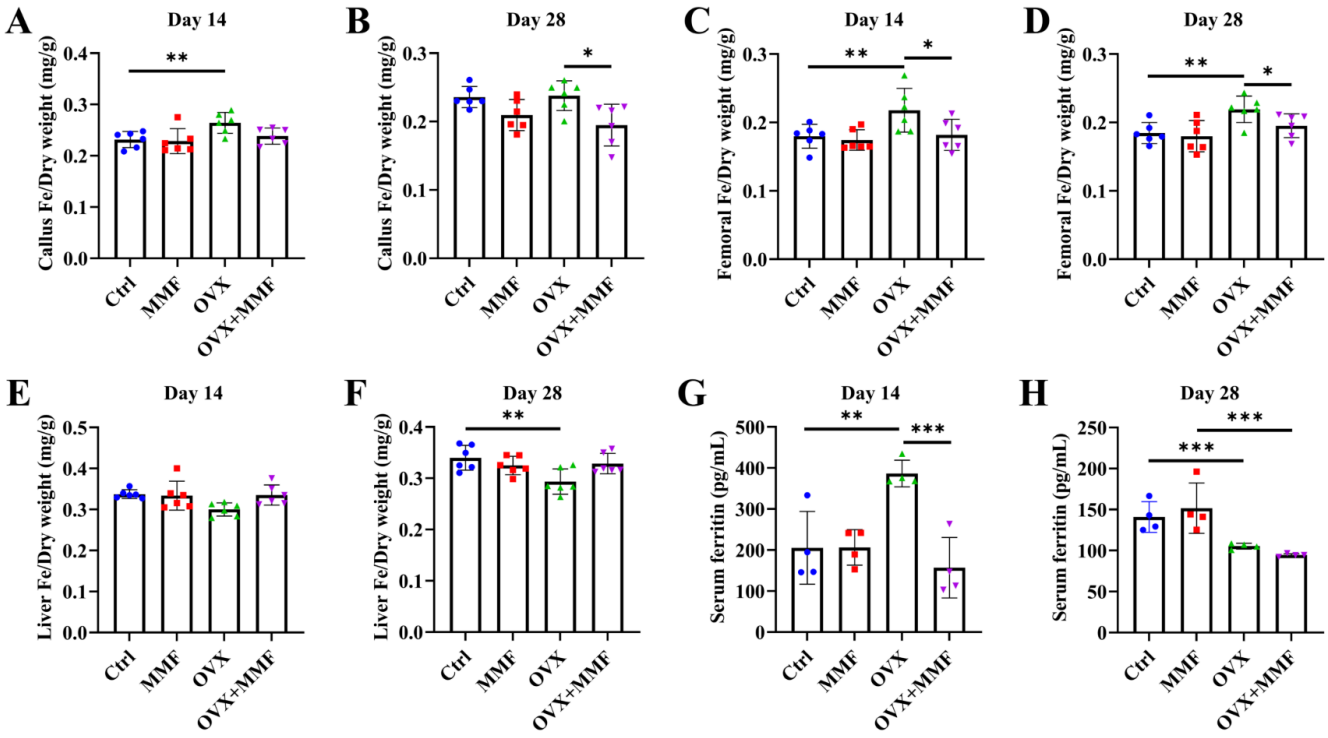


Figure 6

Effects of MMF Exposure on Iron Metabolism in OVX Mice with Tibial Fractures. (A, B) the effect of MMF exposure on iron contents of callus on day 14 (**A**) and day 28 (**B**) days post-tibial fracture in OVX mice. **(C, D)** the effect of MMF exposure on femoral iron content on day 14 (**C**) and day 28 (**D**) days post-tibial fracture in OVX mice. **(E, F)** the effect of MMF exposure on iron contents of liver on day 14 (**E**) and day 28 (**F**) days post-tibial fracture in OVX mice. **(G, H)** the effect of MMF exposure on serum ferritin contents on day 14 (**G**) and day 28 (**H**) days post-tibial fracture in OVX mice. n=6. Data represents the mean ± SD. *P<0.05, **P<0.01 **P<0.001.